

High-order time-accurate, efficient, and structure-preserving numerical methods for the conservative Swift–Hohenberg model



Junxiang Yang^{a,1}, Zhijun Tan^{a,b,1}, Junseok Kim^{c,*}

^a School of Computer Science and Engineering, Sun Yat-sen University, Guangzhou 510275, China

^b Guangdong Province Key Laboratory of Computational Science, Sun Yat-sen University, Guangzhou 510275, China

^c Department of Mathematics, Korea University, Seoul, 02841, Republic of Korea

ARTICLE INFO

Keywords:

Conservative Swift–Hohenberg model
High-order schemes
Energy dissipation
Efficient methods

ABSTRACT

In this study, we develop high-order time-accurate, efficient, and energy stable schemes for solving the conservative Swift–Hohenberg equation that can be used to describe the L^2 -gradient flow based phase-field crystal dynamics. By adopting a modified exponential scalar auxiliary variable approach, we first transform the original equations into an expanded system. Based on the expanded system, the first-, second-, and third-order time-accurate schemes are constructed using the backward Euler formula, second-order backward difference formula (BDF2), and third-order backward difference formula (BDF3), respectively. The energy dissipation law can be easily proved with respect to a modified energy. In each time step, the local variable is updated by solving one elliptic type equation and the non-local variables are explicitly computed. The whole algorithm is totally decoupled and easy to implement. Extensive numerical experiments in two- and three-dimensional spaces are performed to show the accuracy, energy stability, and practicability of the proposed schemes.

1. Introduction

The crystallization is a common phenomenon in nature, industrial, and scientific fields. During this process, the molecules are closely arranged to form crystal structures. The pioneering work of the phase-field modeling for the crystallization can be traced back to Elder et al. [1]. In their work, the concentration of crystal grain is defined using an order parameter ϕ and a total energy functional of ϕ is defined to describe the phase transition. By performing the variational approach of the total energy functional with respect to ϕ , the governing equations of phase-field crystal (PFC) can be derived.

The classical PFC model is highly nonlinear partial differential equation (PDE) and the exact analytic solution is hard to obtain in general. To study the PFC model, accurate and practical numerical methods should be constructed. Li and Kim [2] developed fourth-order spatial-accurate finite difference method (FDM) for the PFC model. Lee and Kim [3] simulated the PFC dynamics on three-dimensional (3D) curved surfaces by using a simple FDM. Dehghan and Mohammadi [4] used the global and local meshless methods to investigate the PFC equation. As a typical H^{-1} -gradient flow problem, the energy dissipation

is a basic property of the PFC model. To satisfy the energy dissipation at numerical level, the structure-preserving methods are required. The convex splitting type methods [5–7] are popular approaches to design energy dissipation-preserving (energy-stable) temporal schemes for gradient flows. Based on the nonlinear convex splitting scheme, Hu et al. [8] constructed energy-stable FDM for the PFC model. Wise et al. [9] later conducted detailed estimations of the convex splitting method for the PFC model. Guan et al. [10] developed energy-stable, hexagonal difference scheme for the two-dimensional (2D) PFC model. Dong et al. [11] studied the convex splitting based second-order time-accurate method for the 3D PFC model and performed error analysis. By combining with the Fourier spectral method, Cheng et al. [12] recently developed fully discrete, energy-stable BDF2 method for the square PFC model. Shin et al. [13] studied the long-time dynamics of PFC equation by combining the convex splitting and high-order Runge–Kutta (RK) methods. Different from the convex splitting method, Pei et al. [14] developed linear, second-order time-accurate, and energy-stable scheme for solving the PFC model, where a proper truncated nonlinear potential was adopted to perform the energy estimation. The recently developed Invariant Energy Quadratization (IEQ) approach provided a novel idea to

* Corresponding author.

E-mail address: cfdkim@korea.ac.kr (J. Kim).

URL: <https://mathematicians.korea.ac.kr/cfdkim> (J. Kim).

¹ Zhijun Tan contributed equally to this work with Junxiang Yang, and is the co-first author for this paper.

<https://doi.org/10.1016/j.camwa.2021.10.016>

Received 2 June 2021; Received in revised form 7 September 2021; Accepted 15 October 2021

design linear schemes. In the original IEQ approach, the original PFC equation was transformed to be equivalent forms by introducing an extra auxiliary variable. To remove some shortcomings of classical IEQ method, Liu and Li [15] proposed modified IEQ method for the PFC model. As an efficient extension of IEQ method, the Scalar Auxiliary Variable (SAV) method was proposed and worked well for PFC model [16] and other gradient flow problems [17–19].

Instead of solving the PFC model directly, we focus on an alternative crystal model which can be derived by combing the variational derivative of Swift–Hohenberg type energy and a Lagrange multiplier enforcing the mass conservation. In this sense, this model is named as the conservative Swift–Hohenberg (CSH) equation. If we remove the Lagrange multiplier from the CSH equation, then the model becomes the classical SH equation. The classical SH model was originally studied by Swift and Hohenberg [20] and it was used for the pattern formations [21,22]. It should be noted that the SH model shares the same free energy functional of Elder’s PFC model. By taking the variational derivative of free energy with respect to phase-field variable in L^2 space, the SH model is obtained and it can be used to describe the localized structure in current physics. During crystallization, the density atoms is modeled by the phase-field function. Therefore, the total mass of phase-field function must be conserved from the perspective of real physics. To force the mass conservation on the SH model and maintain the energy structure, the CSH model can be used to replace the PFC model and describe the dynamics of crystallization. Dehgham and Abbaszadeh [23] developed local meshless method to simulate the SH model. Lee [24] investigated the semi-analytical Fourier spectral method for the SH model. Sarmiento et al. [25] constructed energy dissipation-preserving generalized- α method for the SH model. Su et al. [26] considered a fourth-order spatial-accurate FDM for the SH equation. To construct energy-stable and second-order time-accurate schemes for the generalized SH model, Lee [27] adopted the convex splitting method. Here, a stabilization term was added to perform the energy stability. Liu and Yin [28] proposed efficient linear schemes by coming the IEQ method for temporal discretization and discontinuous Galerkin (DG) method for spatial discretization. Later, various high-order methods based on the RK and SAV methods have been proposed by Liu and Yin [29,30]. To efficiently solve the CSH model, Lee [31] adopted the first- and second-order operator splitting method. In [32], Lee constructed high-order (up to third-order) temporal scheme for the CSH model by using the implicit-explicit RK method. To maintain the energy structure, Zhang and Yang [33] proposed second-order time-accurate scheme for the CSH equation by using the IEQ approach.

Recently, Liu and Li [34] proposed exponential scalar auxiliary variable (ESAV) approach for gradient flows. Later, a modified version of ESAV approach was developed in [35]. Inspired by the modified ESAV approach, we develop high-order time-accurate, efficient, and energy dissipation-preserving methods for solving the CSH model. By using the energy equality derived from the PDE version, we can construct an expanded system consisting of the original equation and energy relation. Based on the expanded system, the time-discretized energy dissipation can be easily estimated. In each time step, only one elliptic type equation needs to be solved. The algorithm is highly efficient and easy to implement.

The rest of this article is organized as follows. In Section 2, we briefly describe the governing equations of SH and CSH models. The derivations of energy dissipation law are introduced. In Section 3, the numerical methods are presented. Extensive numerical simulations are performed in Section 4. The conclusions are given in Section 5.

2. Governing equations

2.1. Swift–Hohenberg equation

We first briefly describe the derivation of SH equation. Let us consider the following free energy functional [20,27]

$$\mathcal{E}(\phi) = \int_{\Omega} \left(G(\phi) - |\nabla\phi|^2 + \frac{1}{2}(\Delta\phi)^2 \right) dx, \tag{1}$$

where $\phi = \phi(t, \mathbf{x})$ is the concentration; and Ω is a smooth, bounded, and connected domain in \mathbb{R}^d , where $d = 1, 2,$ or 3 is the spatial dimension. The nonlinear potential is $G(\phi) = \frac{1}{4}\phi^4 - \frac{g}{3}\phi^3 + \frac{1-\epsilon}{2}\phi^2$, where $g \geq 0$ and $\epsilon \geq 0$ are non-negative constants. By taking the variational approach of Eq. (1) with respect to ϕ , the chemical potential is defined as

$$\mu = \frac{\delta\mathcal{E}}{\delta\phi} = G'(\phi) + 2\Delta\phi + \Delta^2\phi, \tag{2}$$

where δ is used to represent the variational operator, $G'(\phi) = \phi^3 - g\phi^2 + (1 - \epsilon)\phi$ is the derivative of $G(\phi)$ with respect to ϕ . The SH model can be expressed as the L^2 -gradient flow for Eq. (1), i.e.,

$$\frac{\partial\phi}{\partial t} = -\mu, \tag{3}$$

$$\mu = G'(\phi) + 2\Delta\phi + \Delta^2\phi. \tag{4}$$

Here, the periodic boundary condition for ϕ and μ on the domain boundary $\partial\Omega$ is imposed. Let us define the L^2 -inner product of two functionals as $(f^1(\mathbf{x}), f^2(\mathbf{x})) = \int_{\Omega} f^1(\mathbf{x})f^2(\mathbf{x}) dx$ and the L^2 -norm of $f^1(\mathbf{x})$ as $\|f^1(\mathbf{x})\|^2 = (f^1(\mathbf{x}), f^1(\mathbf{x}))$. By taking the L^2 -inner product of Eq. (3) with μ , of Eq. (4) with $\frac{\partial\phi}{\partial t}$, and then summing the results together we have

$$\frac{d}{dt} \mathcal{E}(\phi) = -\|\mu\|^2 \leq 0, \tag{5}$$

where the integration by parts and periodic boundary condition are used. The above inequality indicates the total energy is non-increasing in time (energy dissipation law). By taking the derivative of the total mass with respect to time t , we have

$$\begin{aligned} \frac{d}{dt} \int_{\Omega} \phi dx &= \int_{\Omega} \frac{\partial\phi}{\partial t} dx = - \int_{\Omega} (G'(\phi) + 2\Delta\phi + \Delta^2\phi) dx \\ &= - \int_{\Omega} G'(\phi) dx - 2 \int_{\partial\Omega} \nabla\phi \cdot \mathbf{n} ds - \int_{\partial\Omega} \nabla(\Delta\phi) \cdot \mathbf{n} ds \\ &= - \int_{\Omega} G'(\phi) dx. \end{aligned}$$

Here, \mathbf{n} is the unit outward vector to $\partial\Omega$. In general, $\int_{\Omega} G'(\phi) dx$ is not zero, which implies that the total mass is not conserved.

2.2. Conservative Swift–Hohenberg equation

To preserve the total mass, we should require that $\frac{d}{dt} \int_{\Omega} \phi dx = 0$ holds. In this sense, the CSH model can be constructed as follows

$$\frac{\partial\phi}{\partial t} = -\mu + \frac{1}{|\Omega|} \int_{\Omega} \mu dx, \tag{6}$$

$$\mu = G'(\phi) + 2\Delta\phi + \Delta^2\phi, \tag{7}$$

where $|\Omega| = \int_{\Omega} 1 dx$. By taking the derivative of total mass with respect to time t , we get

$$\frac{d}{dt} \int_{\Omega} \phi dx = \int_{\Omega} \frac{\partial\phi}{\partial t} dx = \int_{\Omega} \left(-\mu + \frac{1}{|\Omega|} \int_{\Omega} \mu dx \right) dx = 0. \tag{8}$$

The above equality indicates the total mass is conserved. By taking the L^2 -inner product of Eq. (6) with μ , we have

$$\begin{aligned} \left(\frac{\partial\phi}{\partial t}, \mu \right) &= - \left(\mu - \frac{1}{|\Omega|} \int_{\Omega} \mu dx, \mu \right) = - \left(\mu - \frac{1}{|\Omega|} \int_{\Omega} \mu dx, \mu - \frac{1}{|\Omega|} \int_{\Omega} \mu dx \right) \\ &\quad - \left(\mu - \frac{1}{|\Omega|} \int_{\Omega} \mu dx, \frac{1}{|\Omega|} \int_{\Omega} \mu dx \right) = - \left\| \mu - \frac{1}{|\Omega|} \int_{\Omega} \mu dx \right\|^2. \end{aligned} \tag{9}$$

By taking the L^2 -inner product of Eq. (7) with $\frac{\partial\phi}{\partial t}$, we have

$$\left(\mu, \frac{\partial \phi}{\partial t}\right) = -\frac{d}{dt} \int_{\Omega} \left(G(\phi) - |\phi|^2 + \frac{1}{2}(\Delta \phi)^2\right) d\mathbf{x}. \tag{10}$$

By summing Eqs. (9) and (10) together, we obtain

$$\begin{aligned} \frac{d}{dt} \mathcal{E}(\phi) &= \frac{d}{dt} \int_{\Omega} \left(G(\phi) - |\phi|^2 + \frac{1}{2}(\Delta \phi)^2\right) d\mathbf{x} \\ &= -\left\| \mu - \frac{1}{|\Omega|} \int_{\Omega} \mu d\mathbf{x} \right\|^2, \end{aligned} \tag{11}$$

where $-\left\| \mu - \frac{1}{|\Omega|} \int_{\Omega} \mu d\mathbf{x} \right\|^2 \leq 0$. Therefore, the above equality indicates that the CSH equation also satisfies the energy dissipation law.

3. Numerical methods

In this section, we construct time-discretized numerical scheme for solving the CSH model. Instead of solving Eqs. (6)–(7) directly, we will consider Eqs. (6)–(7) in an expanded system by using the modified ESAV approach. More precisely, we define the time-dependent variable V to be

$$V = V(t) = \exp\left(\frac{\mathcal{E}(\phi)}{C}\right), \tag{12}$$

where $\mathcal{E}(\phi)$ is the total free energy defined in Eq. (1), C is a large positive constant which is used to suppress the exponential growth. By taking the derivative of V with respect to time t , we get

$$\begin{aligned} \frac{dV}{dt} &= \frac{1}{C} \exp\left(\frac{\mathcal{E}(\phi)}{C}\right) \frac{d}{dt} \mathcal{E}(\phi) = \frac{V}{C} \frac{d}{dt} \mathcal{E}(\phi) \\ &= -\frac{V}{C} \left\| \mu - \frac{1}{|\Omega|} \int_{\Omega} \mu d\mathbf{x} \right\|^2. \end{aligned} \tag{13}$$

Here, the last term holds from Eq. (11). Defining $U = V / \left[\exp\left(\frac{\mathcal{E}(\phi)}{C}\right)\right]$, it can be observed that $U = 1$ always holds in time-continuous case. Next, we expand original equations, Eqs. (6) and (7), to be

$$\frac{\partial \phi}{\partial t} = -\mu + \frac{1}{|\Omega|} \int_{\Omega} \mu d\mathbf{x}, \tag{14}$$

$$\mu = G'(\phi) + 2\Delta \phi + \Delta^2 \phi, \tag{15}$$

$$\frac{dV}{dt} = -\frac{V}{C} \left\| \mu - \frac{1}{|\Omega|} \int_{\Omega} \mu d\mathbf{x} \right\|^2. \tag{16}$$

Here, Eqs. (14) and (15) are indeed the original governing equations and an evolutionary equation with respect to V is added. Because V is a time-dependent variable, we do not need to impose extra boundary condition. The initial value of V can be defined as $V^0 = \exp\left(\frac{\mathcal{E}(\phi^0)}{C}\right)$, where ϕ^0 is the initial value of ϕ . From the definition of V in Eq. (12), we observe $V > 0$ all along, thus $\frac{dV}{dt} \leq 0$ is satisfied from Eq. (16). We now have V is non-increasing in time, and then we conclude that $\mathcal{E}(\phi)$ is also non-increasing because the exponential function is monotonous. In this sense, Eq. (16) provides another approach to estimate the energy dissipation law.

Let $\delta t = T/N_t$ be the uniform time step, T be the final time of computation, N_t be the total number of time iteration, and ϕ^n be the numerical approximation of ϕ at $t = n\delta t$ ($n \leq N$). Based on the expanded system, Eqs. (14)–(16), we now describe the time-discretized schemes.

First-order time-accurate method. By adopting the backward Euler approximation, the first-order time-accurate method for solving Eqs. (14)–(16) can be written as follows:

$$\frac{\bar{\phi} - \phi^n}{\delta t} = -\bar{\mu} + \frac{1}{|\Omega|} \int_{\Omega} \bar{\mu} d\mathbf{x}, \tag{17}$$

$$\bar{\mu} = G'(\phi^n) + 2\Delta \bar{\phi} + \Delta^2 \bar{\phi} + S(\bar{\phi} - \phi^n), \tag{18}$$

$$\frac{V^{n+1} - V^n}{\delta t} = -\frac{V^{n+1}}{C} \left\| \mu^n - \frac{1}{|\Omega|} \int_{\Omega} \mu^n d\mathbf{x} \right\|^2, \tag{19}$$

$$\xi^{n+1} = \frac{V^{n+1}}{\exp\left(\frac{\mathcal{E}(\phi^n)}{C}\right)}, \tag{20}$$

$$\phi^{n+1} = \xi^{n+1} \bar{\phi}. \tag{21}$$

The periodic boundary condition is considered for $\bar{\phi}$. The last term in Eq. (18) plays a role of stabilization and S is a non-negative coefficient. Here, Eq. (17) is generally not easy to solve because the non-local term includes the unknown variables. To achieve efficient computation, we substitute $\bar{\mu}$ in Eq. (17) by Eq. (18) and obtain

$$\begin{aligned} \frac{\bar{\phi} - \phi^n}{\delta t} &= -\left(G'(\phi^n) + 2\Delta \bar{\phi} + \Delta^2 \bar{\phi} + S(\bar{\phi} - \phi^n)\right) \\ &\quad + \frac{1}{|\Omega|} \int_{\Omega} \left(G'(\phi^n) + 2\Delta \bar{\phi} + \Delta^2 \bar{\phi} + S(\bar{\phi} - \phi^n)\right) d\mathbf{x}. \end{aligned} \tag{22}$$

By taking the L^2 -inner product of Eq. (17) with $\mathbf{1}$, we have

$$\frac{1}{\delta t} (\bar{\phi} - \phi^n, \mathbf{1}) = \left(-\bar{\mu} + \frac{1}{|\Omega|} \int_{\Omega} \bar{\mu} d\mathbf{x}, \mathbf{1}\right) = 0, \tag{23}$$

which indicates $\int_{\Omega} \bar{\phi} d\mathbf{x} = \int_{\Omega} \phi^n d\mathbf{x}$. Thus, we can rewrite Eq. (22) as

$$\begin{aligned} \frac{\bar{\phi} - \phi^n}{\delta t} &= -\left(G'(\phi^n) + 2\Delta \bar{\phi} + \Delta^2 \bar{\phi} + S(\bar{\phi} - \phi^n)\right) \\ &\quad + \frac{1}{|\Omega|} \int_{\Omega} \left(G'(\phi^n) + S(\phi^n - \phi^n)\right) d\mathbf{x} + \frac{1}{|\Omega|} \int_{\partial \Omega} (2\nabla \bar{\phi} + \nabla(\Delta \bar{\phi})) \cdot \mathbf{n} ds \\ &= -\left(G'(\phi^n) + 2\Delta \bar{\phi} + \Delta^2 \bar{\phi} + S(\bar{\phi} - \phi^n)\right) + \frac{1}{|\Omega|} \int_{\Omega} G'(\phi^n) d\mathbf{x}, \end{aligned} \tag{24}$$

where the divergence theorem and periodic boundary condition are used. Now, the non-local term only contains the known variable computed from the previous step and it can be treated as a source term. It can be observed that Eq. (24) is a linear scheme with constant coefficients, $\bar{\phi}$ can be easily updated by calculating an elliptic type equation with any fast solver. Therefore, the proposed method is highly efficient.

Next, we need to update V^{n+1} . Eq. (19) can be recast to be

$$V^{n+1} = \frac{V^n}{1 + \frac{\delta t}{C} \left\| \mu^n - \frac{1}{|\Omega|} \int_{\Omega} \mu^n d\mathbf{x} \right\|^2}. \tag{25}$$

Because $\left\| \mu^n - \frac{1}{|\Omega|} \int_{\Omega} \mu^n d\mathbf{x} \right\|^2$, δt , and C are all non-negative, we can easily check V^1 is non-negative if we choose the initial value $V^0 \geq 0$. By the recursion, we can obtain non-negative V^{n+1} , V^n , V^{n-1} , ... From Eq. (19), we conclude that $V^{n+1} \leq V^n$ and more importantly,

$$C \ln(V^{n+1}) \leq C \ln(V^n), \tag{26}$$

which implies the time-discretized energy dissipation law with respect to a modified energy $C \ln(V)$.

With the computed V^{n+1} from Eq. (25), we can directly obtain ξ^{n+1} from Eq. (20). Finally, we update ϕ^{n+1} from Eq. (21). The computation in one time step is completed. As we can observe, the computational cost mainly comes from the calculation for $\bar{\phi}$. The whole algorithm is not only very easy to implement but also follows the energy dissipation property in time-discretized version.

Second-order time-accurate scheme. By using the BDF2 approximation, the second-order time-accurate scheme for solving Eqs. (14)–(16) can be written as follows:

$$\frac{3\tilde{\phi} - 4\phi^n + \phi^{n-1}}{2\delta t} = -\tilde{\mu} + \frac{1}{|\Omega|} \int_{\Omega} \tilde{\mu} \, d\mathbf{x}, \tag{27}$$

$$\tilde{\mu} = G'(\phi^*) + 2\Delta\tilde{\phi} + \Delta^2\tilde{\phi} + S(\tilde{\phi} - \phi^*), \tag{28}$$

$$\frac{V^{n+1} - V^n}{\delta t} = -\frac{V^{n+1}}{C} \left\| \mu^* - \frac{1}{|\Omega|} \int_{\Omega} \mu^* \, d\mathbf{x} \right\|^2, \tag{29}$$

$$\xi^{n+1} = \frac{V^{n+1}}{\exp\left(\frac{\mathcal{E}(\phi^*)}{C}\right)}, \tag{30}$$

$$\phi^{n+1} = \xi^{n+1}(2 - \xi^{n+1})\tilde{\phi}, \tag{31}$$

where $\phi^* = 2\phi^n - \phi^{n-1}$ and $\mu^* = 2\mu^n - \mu^{n-1}$ are the second-order extrapolations. By using a similar approach described for the first-order time-accurate scheme, we can calculate $\tilde{\phi}$ by substituting $\tilde{\mu}$ in Eq. (27) by Eq. (28). Next, V^{n+1} and ξ^{n+1} are computed from Eqs. (29) and (30), respectively.

Note that V^{n+1} is computed by a first-order scheme, i.e., $V^{n+1} = V^n + O(\delta t)$, then we have

$$\xi^{n+1} = \xi^n + C^1 \delta t = 1 + C^1 \delta t, \tag{32}$$

where C^1 is a constant, and then we get

$$\xi^{n+1}(2 - \xi^{n+1}) = (1 + C^1 \delta t)(1 - C^1 \delta t) = 1 - (C^1)^2 \delta t^2, \tag{33}$$

which indicates $\xi^{n+1}(2 - \xi^{n+1})$ is a second-order approximation of 1. By using the similar procedure described for first-order time-accurate scheme, we have the time-discretized energy dissipation law in the sense that $V^{n+1} \leq V^n$ and more importantly,

$$C \ln(V^{n+1}) \leq C \ln(V^n). \tag{34}$$

Third-order time-accurate method. By using the BDF3 approximation, the third-order time-accurate method for solving Eqs. (14)–(16) can be written as follows:

$$\frac{11\tilde{\phi} - 18\phi^n + 9\phi^{n-1} - 2\phi^{n-2}}{6\delta t} = -\tilde{\mu} + \frac{1}{|\Omega|} \int_{\Omega} \tilde{\mu} \, d\mathbf{x}, \tag{35}$$

$$\tilde{\mu} = G'(\phi^*) + 2\Delta\tilde{\phi} + \Delta^2\tilde{\phi} + S(\tilde{\phi} - \phi^*), \tag{36}$$

$$\frac{V^{n+1} - V^n}{\delta t} = -\frac{V^{n+1}}{C} \left\| \mu^* - \frac{1}{|\Omega|} \int_{\Omega} \mu^* \, d\mathbf{x} \right\|^2, \tag{37}$$

$$\xi^{n+1} = \frac{V^{n+1}}{\exp\left(\frac{\mathcal{E}(\phi^*)}{C}\right)}, \tag{38}$$

$$\phi^{n+1} = \xi^{n+1}(3 - 3\xi^{n+1} + (\xi^{n+1})^2)\tilde{\phi}, \tag{39}$$

where $\phi^* = 3\phi^n - 3\phi^{n-1} + \phi^{n-2}$ and $\mu^* = 3\mu^n - 3\mu^{n-1} + \mu^{n-2}$ are the third-order extrapolations. Similarly, we calculate $\tilde{\phi}$ by substituting $\tilde{\mu}$ in Eq. (35) by Eq. (36). Then, V^{n+1} and ξ^{n+1} are updated from Eqs. (37) and (38), respectively.

From

$$\xi^{n+1} = \xi^n + C^1 \delta t = 1 + C^1 \delta t, \tag{40}$$

we have

$$\begin{aligned} \xi^{n+1}(3 - 3\xi^{n+1} + (\xi^{n+1})^2) &= [1 - (1 - \xi^{n+1})][1 + (1 - \xi^{n+1}) + (1 - \xi^{n+1})^2] \\ &= (1 - C^1 \delta t)[1 + C^1 \delta t + (C^1 \delta t)^2] \\ &= 1 - (C^1)^3 \delta t^3, \end{aligned} \tag{41}$$

which indicates $\xi^{n+1}(3 - 3\xi^{n+1} + (\xi^{n+1})^2)$ is a third-order approximation of 1. By the similar process, we get the time-discretized energy dissipation law in the sense that $V^{n+1} \leq V^n$ and more importantly,

$$C \ln(V^{n+1}) \leq C \ln(V^n). \tag{42}$$

Table 1

Errors and convergence rates with respect to the second- and third-order schemes.

δt	BDF2	Order	BDF3	Order
2^{-3}	1.00e-0	–	4.20e-1	–
2^{-4}	2.88e-1	1.79	4.34e-2	3.27
2^{-5}	6.35e-2	2.18	5.90e-3	2.88
2^{-6}	1.53e-2	2.05	7.30e-4	3.01

Remarks. In this section, several time-discretized numerical schemes for solving the CSH model are proposed. In each time step, we update $\tilde{\phi}$ by solving an elliptic type equation with constant coefficients. The unique solvability can be estimated by the Lax–Milgram theorem [36,37] or minimization of convex energy functional [27,38]. Other non-local variables can be directly updated by explicit manners. Therefore, the numerical methods are highly efficient and easy to implement. When we use high-order scheme (BDF2 or BDF3) to perform the computation, the previous information is needed. In this work, we use first-order backward Euler scheme to compute the variable at first time step, and then the BDF2 is used to compute the variable at second time step. With the known variables at previous two time steps, the BDF3 scheme is used from the third time step. This procedure can maintain the energy stability from the initial state to the final time because we have proved that backward Euler, BDF2, and BDF3 satisfy the energy dissipation law. If one wants to consistently guarantee the high-order accuracy, the third-order Runge–Kutta method may be an appropriate choice to compute the variables at first and second time steps. The present work only focuses on a novel numerical approach for the CSH model and the numerical results in the next section show that the proposed schemes are practical. In a separate work, the convergence and error estimations of the proposed methods will be investigated in detail.

4. Numerical experiments

We perform extensive computational experiments to validate the proposed schemes. The spatial discretization is performed by using the Fourier-spectral method [39]. Unless otherwise stated, we use $S = 2$ and $C = 1e6$.

4.1. Temporal accuracy

We first demonstrate the high-order (second- and third-order) temporal accuracies of the proposed methods. The domain is $\Omega = (0, 32)$ and the space step is $h = 1/3$. The following initial condition is considered

$$\phi(x, y, 0) = \sin\left(\frac{\pi x}{16}\right). \tag{43}$$

We set $g = 0$ and $\epsilon = 0.025$. The reference solution is obtained by using the third-order scheme with smaller time step $\delta t = 2^{-12}$. To investigate the convergence rates with respect to different time steps, we choose $\delta t = 2^{-3}, 2^{-4}, 2^{-5}$, and 2^{-6} to perform the simulations. The numerical errors and convergence rates at $T = 1$ with respect to second-order and third-order schemes are listed in Table 1. It is observed that high-order scheme obviously reduces the errors and accelerates the convergence.

4.2. Energy dissipation

As described in Section 3, the solutions of numerical schemes follow the energy dissipation property with respect to modified energy. To validate this, we consider the pattern formation with the following initial condition [27]

$$\begin{aligned} \phi(x, y, 0) &= 0.07 - 0.02 \cos\left(\frac{\pi(x-12)}{16}\right) \sin\left(\frac{\pi(y-1)}{16}\right) \\ &\quad + 0.02 \cos^2\left(\frac{\pi(x+10)}{32}\right) \sin^2\left(\frac{\pi(y+3)}{32}\right) \end{aligned}$$

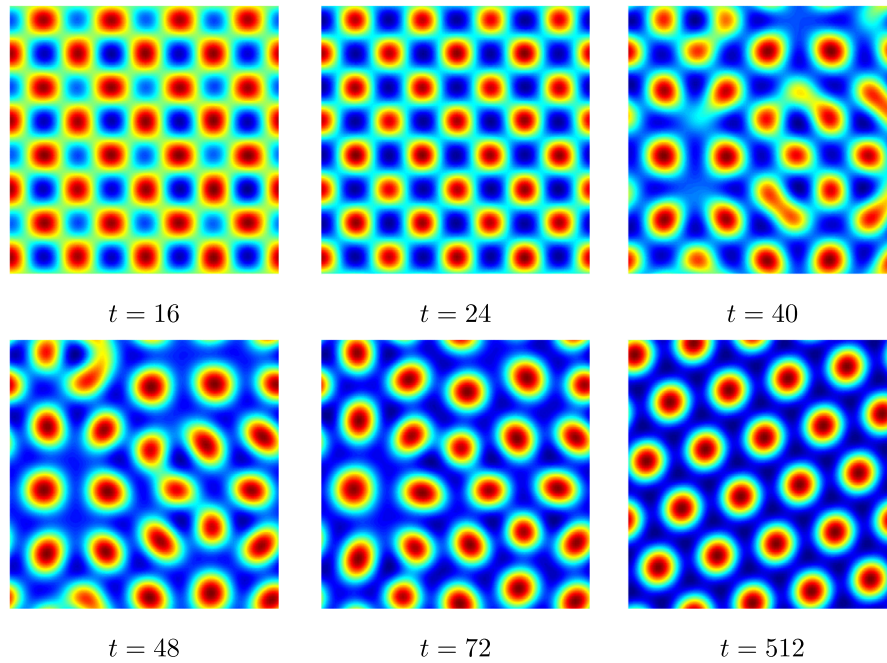


Fig. 1. The pattern at different moments. Here, the results are computed by the third-order accurate scheme with $\delta t = 0.0625$.

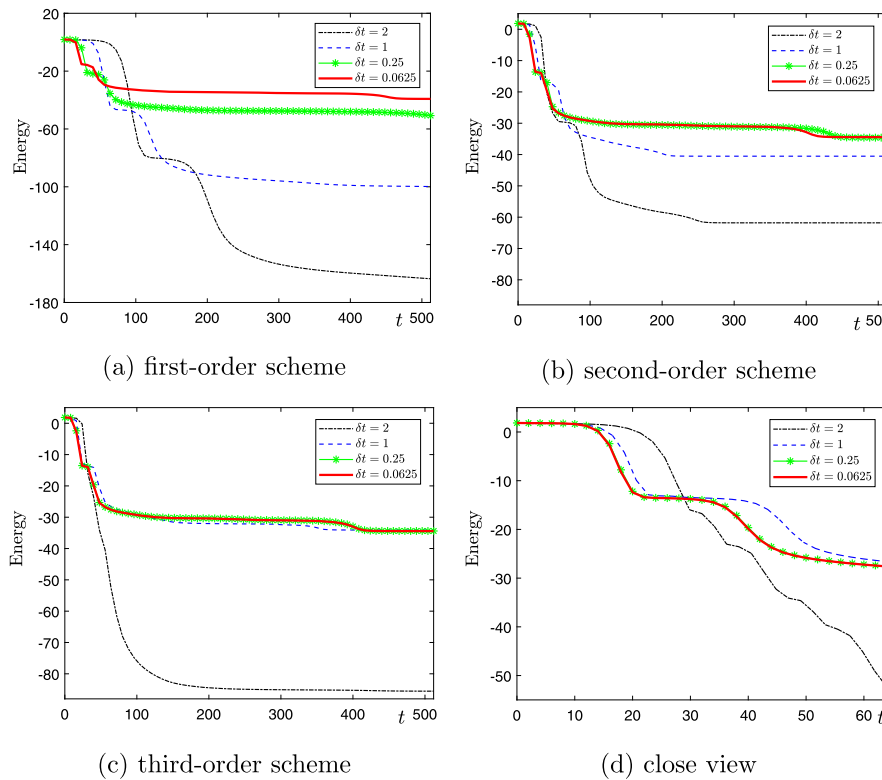


Fig. 2. The energy curves computed by (a) first-, (b) second-, and (c) third-order accurate schemes. Here, (d) is a close view of (c).

$$-0.01 \sin^2\left(\frac{\pi x}{8}\right) \sin^2\left(\frac{\pi(y-6)}{8}\right) \tag{44}$$

in the domain $\Omega = (0, 32)^2$. Here, we set $g = 1$, $\epsilon = 0.25$, grid size $h = 1/3$. The simulations are performed by using the first-, second-, and third-order accurate schemes with different time steps $\delta t = 2, 1, 0.25$, and 0.0625 . Fig. 1 illustrates the snapshots computed by the third-order accurate scheme with finer time step $\delta t = 0.0625$. The present results are qualitatively similar with previous simulation in [27]. The evolu-

tions of energy curves computed by the first-, second-, and third-order accurate schemes are plotted in Figs. 2(a), (b), and (c), respectively. Fig. 2(d) shows a close view of (c). As we can see, the energy curves are non-increasing in time even if larger time step is used. Moreover, the high-order accurate scheme obviously speeds up the convergence of energy curve as the refinement of time step. Although the energy curves are non-increasing for relatively large time steps, we note that the good energy stability does not guarantee the desired computational

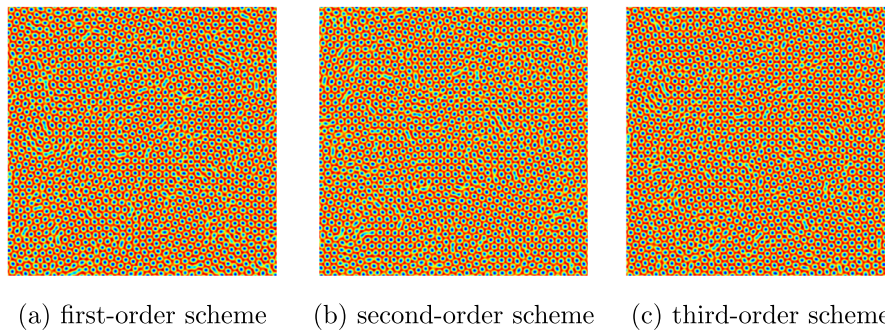


Fig. 3. The pattern profiles computed by (a) first-, (b) second-, and (c) third-order accurate schemes.

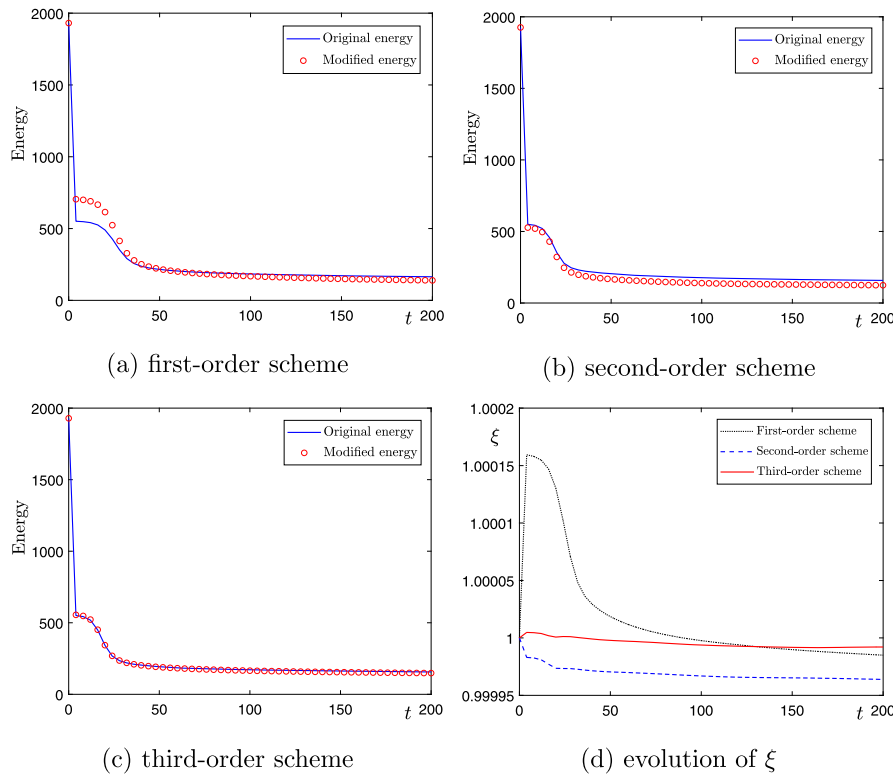


Fig. 4. Evolution of original energy and modified energy computed by (a) first-, (b) second-, and (c) third-order accurate schemes. Here, (d) shows the evolution of ξ .

accuracy simultaneously. The results indicate that a small enough time step is still necessary if we want to obtain an accurate and convergent result.

4.3. Effect of numerical scheme

In general, the high-order time-accurate scheme can obtain more accurate and desired result when we use a relatively fine time step. To compare the effect of different schemes on the simulation, we consider the phase transition in the domain $\Omega = (0, 256)^2$. The initial condition is defined as

$$\phi(x, y, 0) = 0.15 + 0.1\text{rand}(x, y), \tag{45}$$

where $\text{rand}(x, y)$ is the random value locating at $[-1, 1]$. Here, we use $\delta t = 0.1$, grid size $h = 1$, $\epsilon = 0.25$, and $g = 0$. In Figs. 3(a), (b), and (c), we plot the results at $T = 200$ computed by the first-, second-, and third-order accurate schemes, respectively. As we can see, the pattern profiles are very similar. To further compare the three schemes, we consider the evolutions of original energy functional defined in Eq. (1) and modified

energy functional $C \ln(V)$. From the results shown in Figs. 4(a), (b), and (c), we find that the original and modified energy curves computed by the high-order scheme are very consistent. Furthermore, we also plot the evolutions of ξ computed by three numerical schemes in Fig. 4(d). Note that ξ is a time-dependent variable, we define $\max(|\xi^n - 1|_{t^n \in [0, T]})$ as a criterion to measure the difference between numerical and exact values. The results indicate that the numerical value of ξ is close to the desired value, i.e., $\xi = 1$ when we use high-order scheme.

4.4. Comparison between the SH and CSH models

The classical SH model without mass conservation is a widely used model for simulating pattern formations [22,27]. The CSH model considered in this work is a practical choice for simulating the phase-field crystal dynamics in the sense of L^2 -gradient flow. In this subsection, we compare the different dynamics between the SH model and CSH model. The domain is $\Omega = (0, 256)^2$. The initial condition is set to be

$$\phi(x, y, 0) = \bar{\phi} + 0.1\text{rand}(x, y), \tag{46}$$

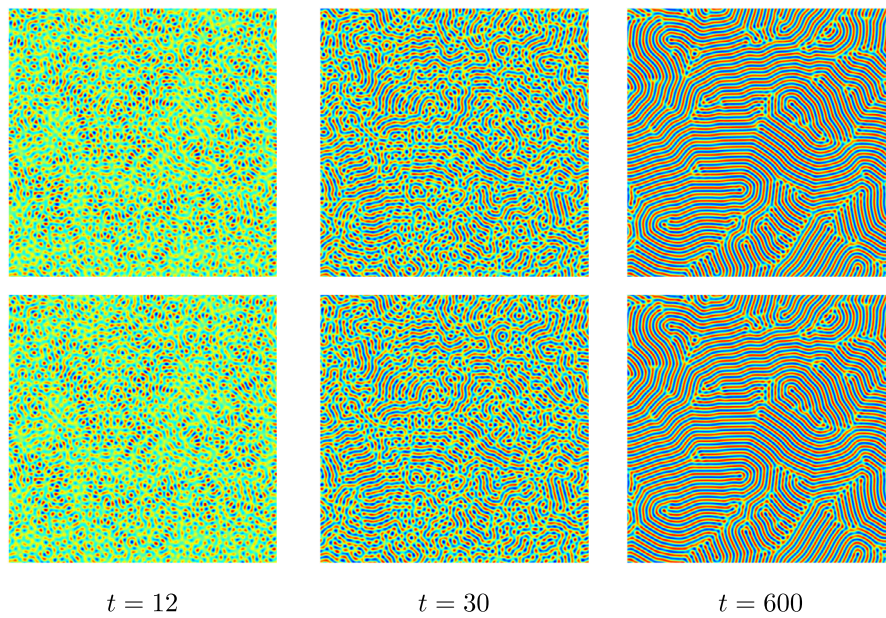


Fig. 5. The formation of striped pattern. Here, $\bar{\phi} = 0$, the top and bottom rows display the results computed by the SH and CSH model, respectively.

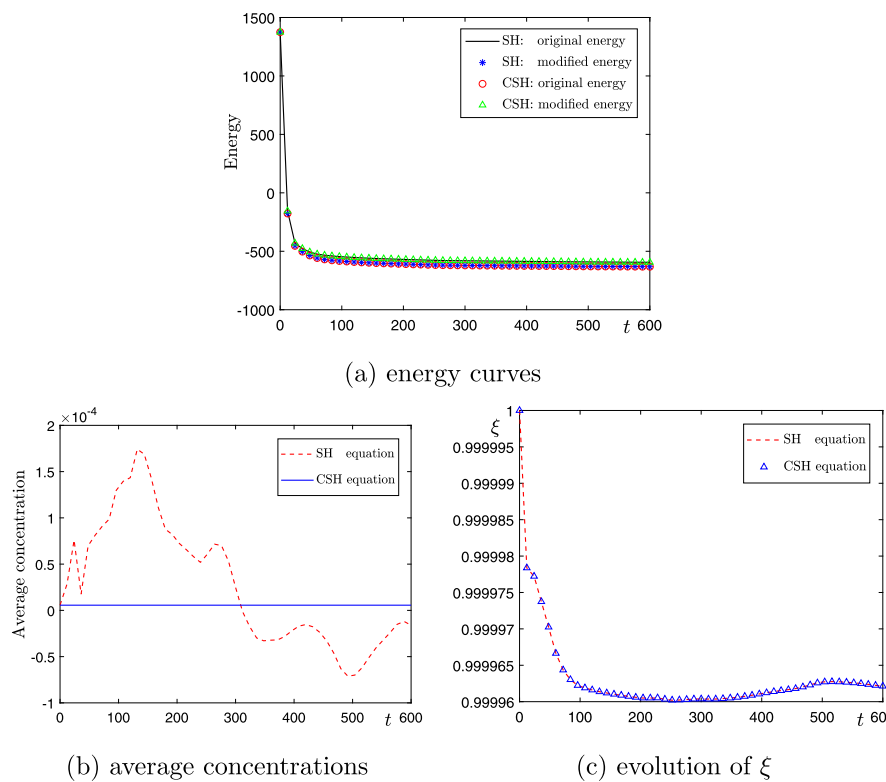


Fig. 6. The evolutions of (a) energy curves, (b) average concentrations, and (c) ξ with $\bar{\phi} = 0$.

where $\bar{\phi}$ is the average concentration. Here, we use $\Delta t = 0.2$, $h = 1$, $\epsilon = 0.25$, and $g = 0$. For the H^{-1} -gradient flow based phase-field crystal model, the striped and hexagonal patterns with respect to different values of $\bar{\phi}$ [2,3,13]. In the present simulations, we choose $\bar{\phi} = 0$ and $\bar{\phi} = 0.15$. The top and bottom rows of Fig. 5 display the snapshots computed by the SH and CSH models with $\bar{\phi} = 0$, respectively. We find that striped pattern appear and the results are very similar. In Figs. 6(a), (b), and (c), we plot the evolutions of energy, average concentrations, and ξ . The results indicate that the energy curves

are non-increasing, the average concentration of CSH model is conserved, the values of ξ are close to 1. The top and bottom rows of Fig. 7 show the snapshots computed by the SH and CSH models with $\bar{\phi} = 0.15$, respectively. It is observed that the CSH model leads to hexagonal pattern while the SH model still leads to striped pattern. The evolutions of energy, average concentrations, and ξ are plotted in Figs. 8(a), (b), and (c), respectively. The comparison study indicates that the average concentration obviously affects the dynamics of CSH model.

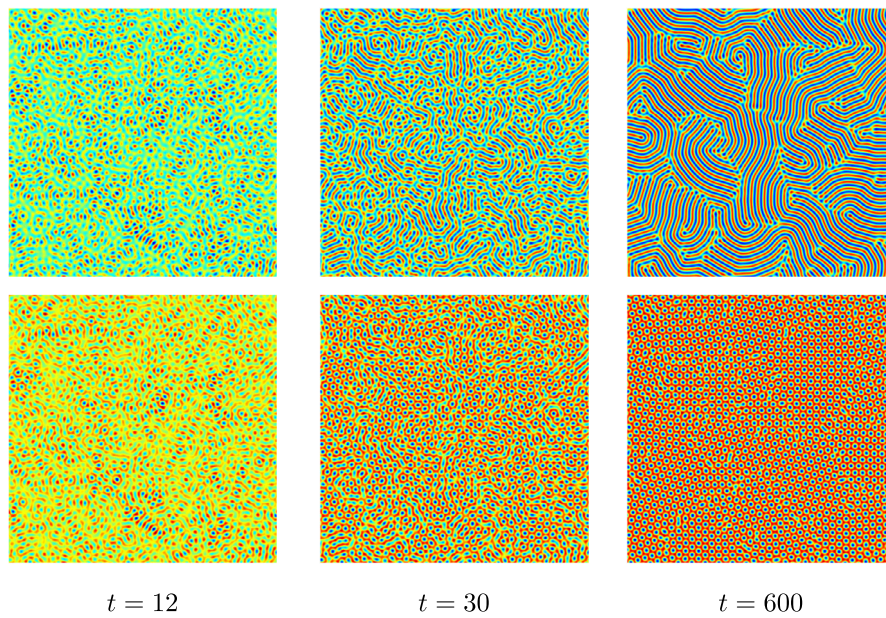


Fig. 7. The formation of striped pattern. Here, $\bar{\phi} = 0.15$, the top and bottom rows display the results computed by the SH and CSH model, respectively.

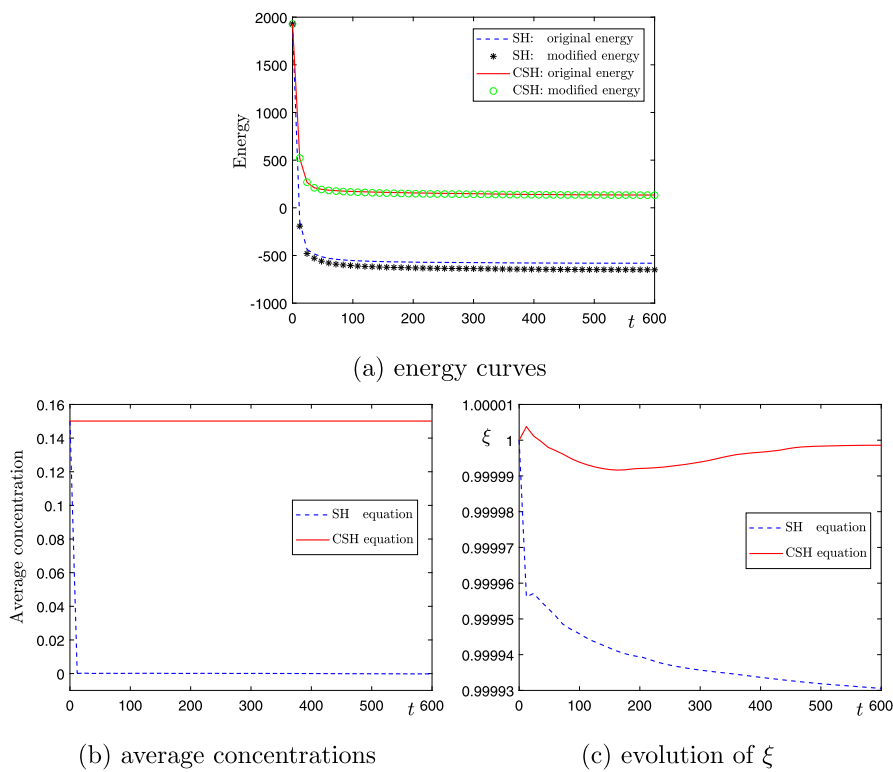


Fig. 8. The evolutions of (a) energy curves, (b) average concentrations, and (c) ξ with $\bar{\phi} = 0.15$.

4.5. Crystallization

Let us consider the small crystal nuclei which are placed in the ambient liquid. The initial perturbations drives the growth of crystal and the crystal patterns eventually spread all over the domain. This process is called as the crystallization [2,3,31,33,40]. To investigate the effect of initial state on the crystallization, we use

$$\phi(x_l, y_l, 0) = 0.285 + 0.446 \left(\cos \left(\frac{0.66}{\sqrt{3}} y_l \right) \cos(0.66x_l) - 0.5 \cos \left(\frac{1.32}{\sqrt{3}} y_l \right) \right) \quad (47)$$

in the domain $\Omega = (0, 400)^2$. The local coordinates are

$$\begin{aligned} x_l &= x \sin \theta + y \cos \theta, \\ y_l &= -x \cos \theta + y \sin \theta. \end{aligned}$$

In the first case, an initial patch with length 30 locates in (185, 165) with $\theta = 0.25\pi$. Fig. 9 displays the snapshots of crystal growth starting from one nucleus. As we can observe from final stage, the crystal pattern spreads over the domain in an almost uniform manner. In the second case, three initial patches with length 30 locate in (185, 165), (165, 235), (235, 215) with $\theta = 0.25\pi, 0$, and -0.25π . The snapshots of crystal growth

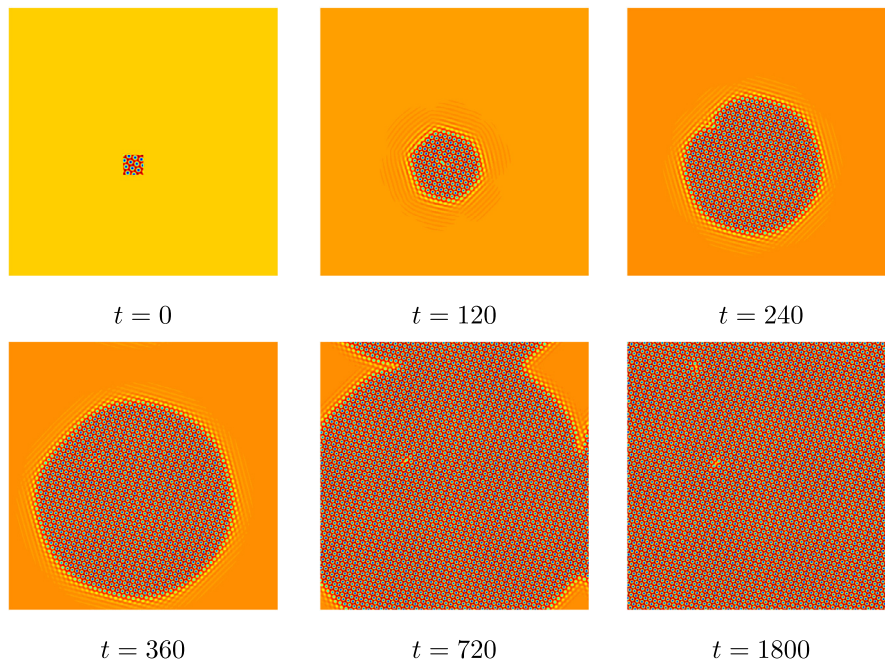


Fig. 9. Crystal growth with only one nucleus.

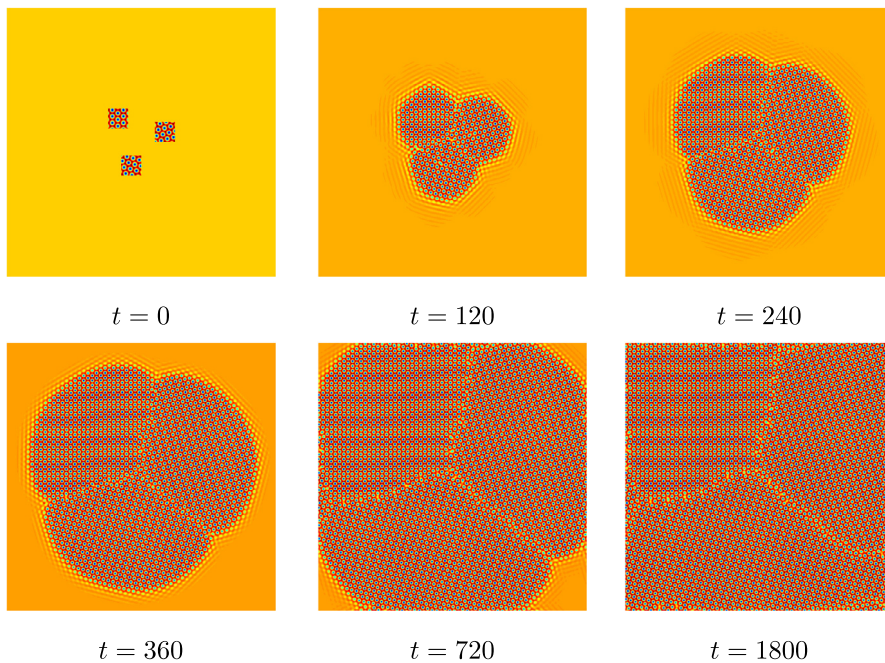


Fig. 10. Crystal growth with three nucleuses.

starting from three nucleuses are shown in Fig. 10. At final stage, the grain boundaries can be observed. This describes the formation of defects in natural crystals. In Figs. 11(a), (b), and (c), the evolutions of energy, average concentrations, and ξ are plotted. We find that the energy curves are dissipative, average concentrations are conserved, and the values of ξ are close to 1.

4.6. Effects of $\bar{\phi}$ and g

For a generalized phase-field crystal model, the average concentration $\bar{\phi}$ and cubic term (i.e., the value of g) significantly affect the dynamics of pattern formation. In this part, we choose three pairs of parameters $(\bar{\phi}, g) = (0, 0)$, $(0.16, 0)$, and $(0, 1)$ to perform the simulations in

$\Omega = [0, 256]^2$. Here, we set $\Delta t = 0.2$, $h = 1$, $\epsilon = 0.25$. The top, middle, and bottom rows of Fig. 12 display the results computed with $(\bar{\phi}, g) = (0, 0)$, $(0.16, 0)$, and $(0, 1)$, respectively. As $(\bar{\phi}, g) = (0, 0)$, the striped pattern is observed. As $(\bar{\phi}, g) = (0.16, 0)$ or $(0, 1)$, we can observe the formation of hexagonal pattern. From the results plotted in Figs. 13(a), (b), and (c), we find that the energy curves are dissipative, average concentrations are conserved, and the values of ξ are close to 1.

Next, we consider the phase transition in three-dimensional domain $\Omega = (0, 128)^3$. The initial condition is defined as

$$\phi(x, y, z, 0) = 0.1 \text{rand}(x, y, z). \tag{48}$$

Here, we use $\Delta t = 1.28$, $h = 1$, $\epsilon = 0.25$ and $g = 0$ and 1 to perform the simulations. The snapshots at different moments are shown in Figs. 14

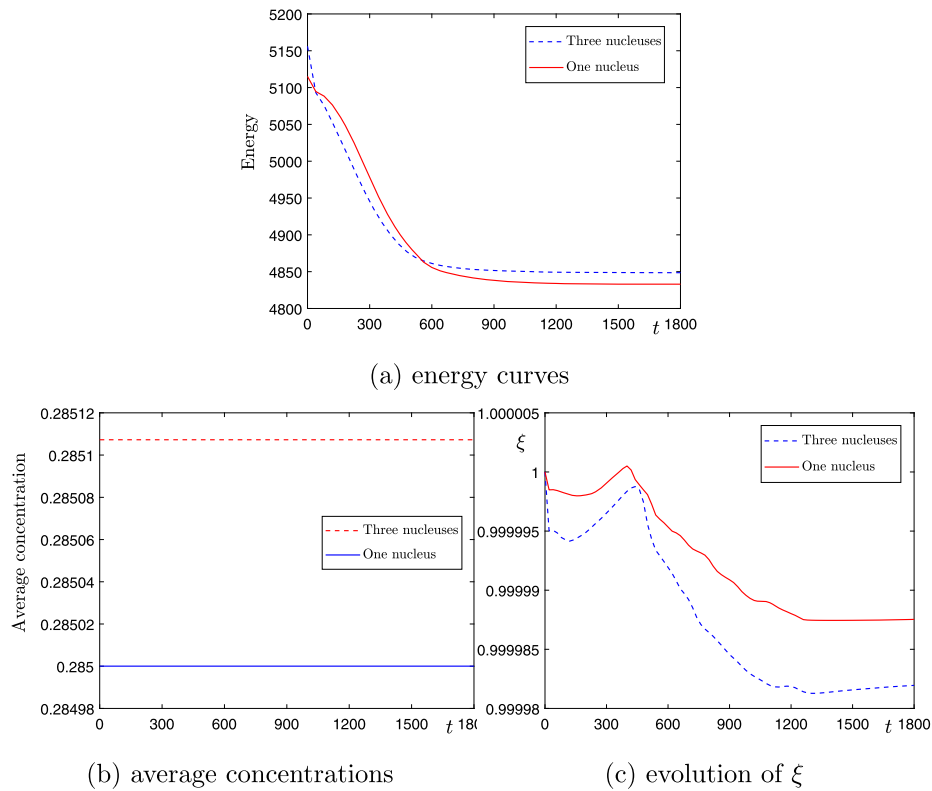


Fig. 11. The evolutions of (a) energy curves, (b) average concentrations, and (c) ξ in crystal growth.

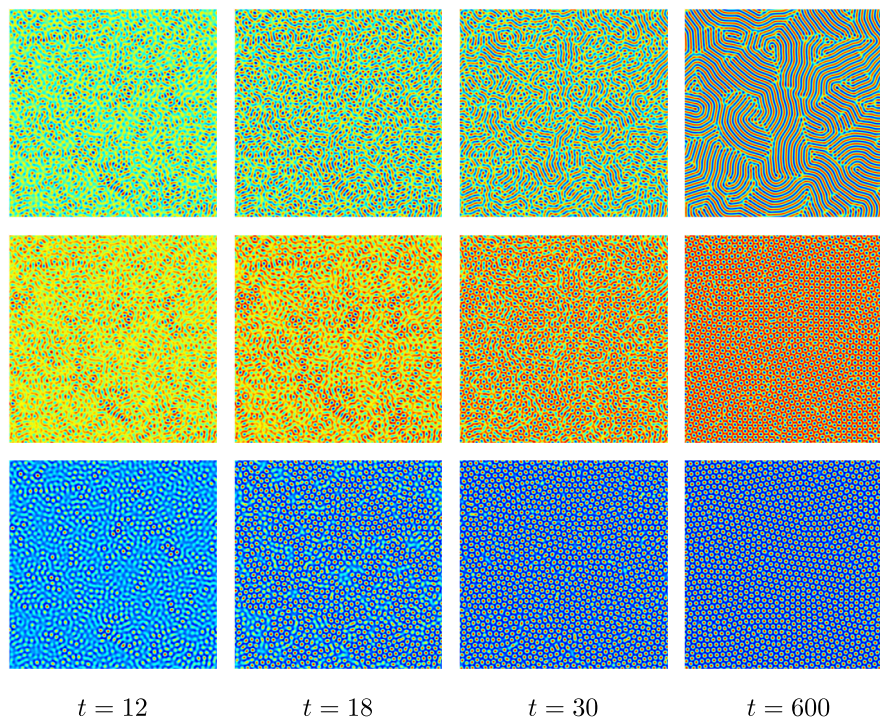


Fig. 12. Pattern formations with $(\bar{\phi}, g) = (0, 0)$ (top row), $(\bar{\phi}, g) = (0.16, 0)$ (middle row), $(\bar{\phi}, g) = (0, 1)$ (bottom row).

and 15. Here, the sectional views correspond to $x = 64$ and $z = 64$. As we can observe, the striped and hexagonal patterns appear with respect to $g = 0$ and $g = 1$. In Fig. 16, the left column illustrates the contour surfaces ($\phi = 0$) at $t = 768$ and right column displays the corresponding close views. The evolutions of energy and ξ are plotted in Fig. 17. The energy curves are non-increasing in time and the values of ξ are close to 1.

4.7. Effects of $\bar{\phi}$ and ϵ

Depending on the values of $\bar{\phi}$ and ϵ , the phase diagram of crystal model involves striped, hexagonal, and constant regions. Elder et al. [1] first plotted the distributions of patterns with respect to average concentration and ϵ (see Fig. 18(a)). Lee [32] plotted the two-dimensional

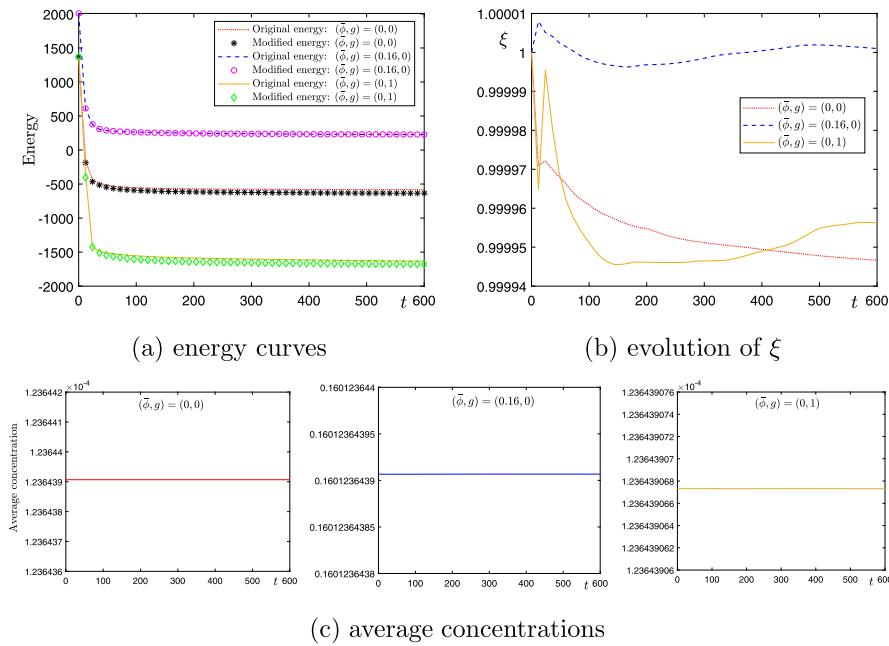


Fig. 13. The evolutions of (a) energy curves, (b) ξ . Here, (c) displays the evolutions of average concentration with respect to $(\bar{\phi}, g) = (0, 0)$, $(0.16, 0)$, and $(0, 1)$ (from the left to right).

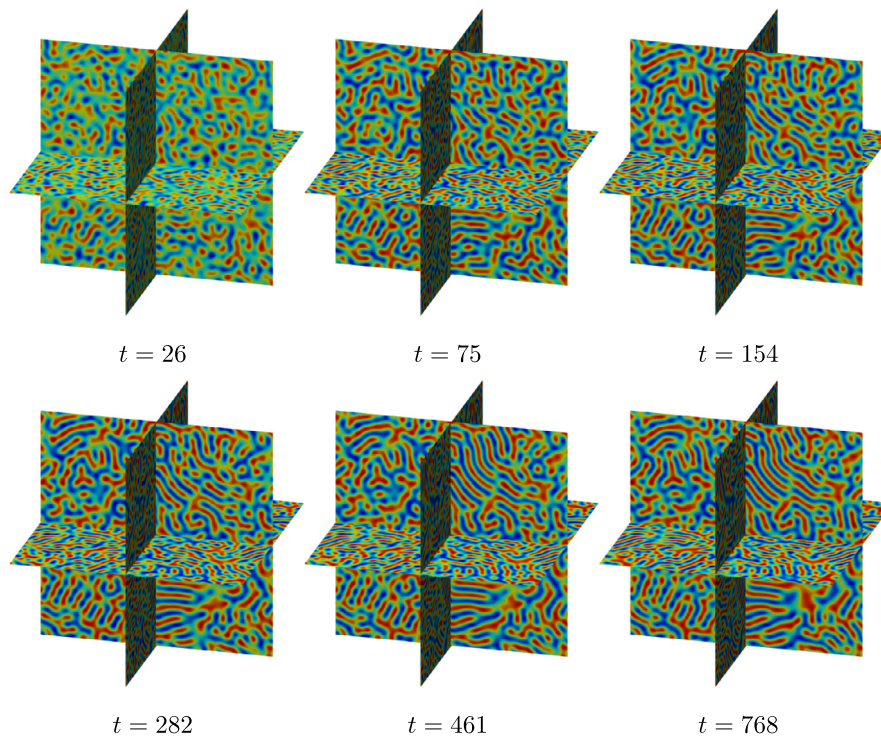


Fig. 14. Three-dimensional phase transition with $g = 0$.

phase diagram of a CSH model with respect to the values of $\bar{\phi}$ and ϵ (see Fig. 18(b)).

In this subsection, we simulate the striped, hexagonal, and constant patterns by choosing specific parameters shown in the phase diagram (Fig. 18(b)). The initial condition is defined as

$$\phi(x, y, 0) = \bar{\phi} + 0.1\text{rand}(x, y). \tag{49}$$

The domain is $\Omega = (0, 32)^2$. We use $\Delta t = 0.2$, $h = 1/3$, $g = 0$. The time-dependent indicator function is defined to be [1,32]

$$\Lambda(t) = \begin{cases} \int_{\Omega} |\phi - \bar{\phi}| \, d\mathbf{x} & \text{if } \int_{\Omega} |\nabla(\phi - \bar{\phi})| \, d\mathbf{x} \leq 1e-10, \\ \frac{\int_{\Omega} |\phi - \bar{\phi}| \, d\mathbf{x}}{\int_{\Omega} |\nabla(\phi - \bar{\phi})| \, d\mathbf{x}} & \text{otherwise.} \end{cases} \tag{50}$$

Here, we choose $(\bar{\phi}, \epsilon) = (0.02, 0.1)$, $(0.14, 0.1)$, and $(0.26, 0.1)$ to perform the simulations. The top row of Fig. 19 illustrates the snapshots of the case $(\bar{\phi}, \epsilon) = (0.02, 0.1)$, we can observe the formation of striped pattern. In the middle and bottom rows of Fig. 19, the results with $(\bar{\phi}, \epsilon) = (0.14, 0.1)$ and $(0.26, 0.1)$ are shown. As we can see, the hexago-

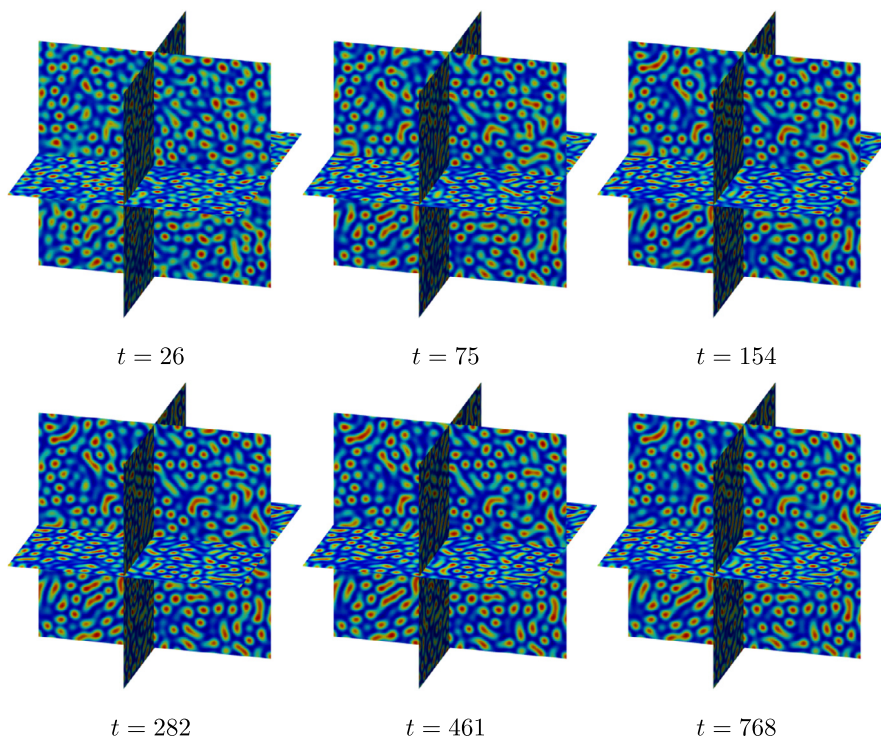


Fig. 15. Three-dimensional phase transition with $g = 1$.

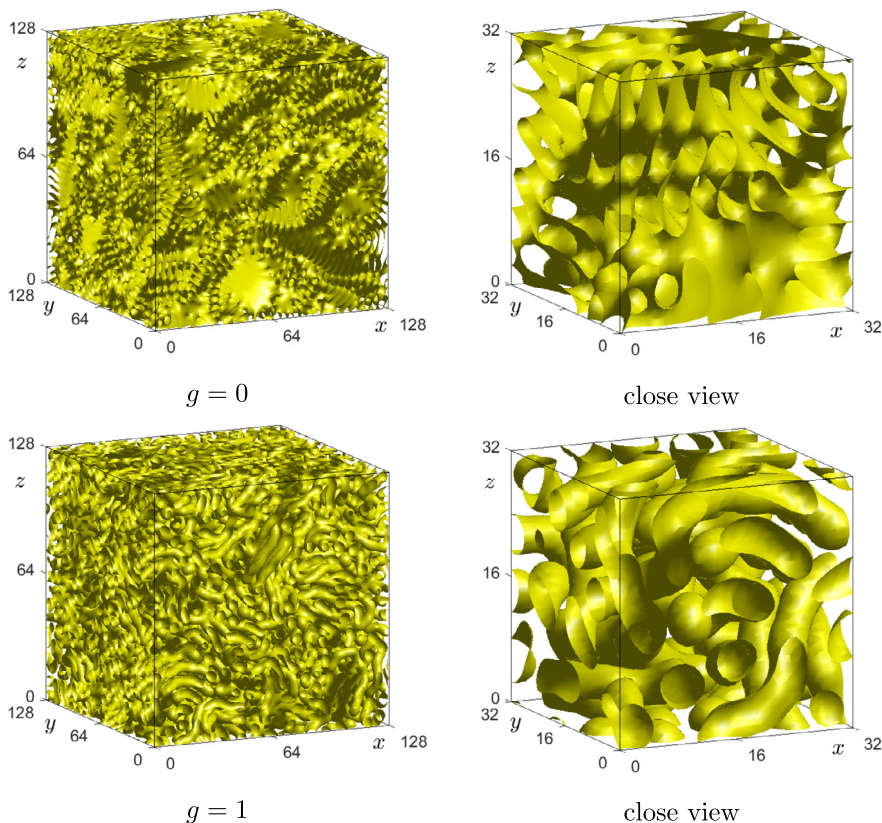


Fig. 16. Contour surface ($\phi = 0$) at $t = 768$ with respect to $g = 0$ (top row) and $g = 1$ (bottom row). Here, the right column displays the close views.

nal and constant patterns evolves, respectively. In Fig. 20, we plot the evolutions of $\Lambda(t)$. As described in [32], the solution evolves to a constant value, i.e., $\int_{\Omega} |\phi - \bar{\phi}| dx \approx 0$ and $\int_{\Omega} |\nabla(\phi - \bar{\phi})| dx \approx 0$. In this sense, $\Lambda(t)$ is evaluated by using $\int_{\Omega} |\phi - \bar{\phi}| dx$ and the value is close to zero.

5. Conclusions

In this article, several efficient and energy-stable time-discretized schemes were proposed for solving the CSH model. Instead of comput-

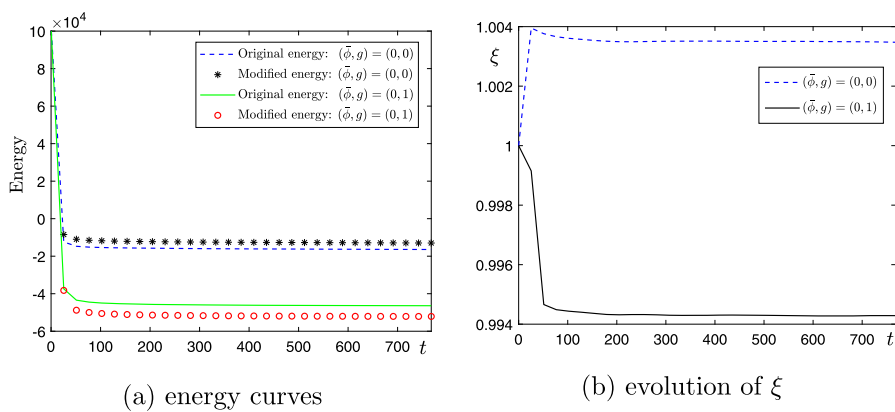


Fig. 17. The evolutions of (a) energy curves and (b) ξ in three-dimensional domain.

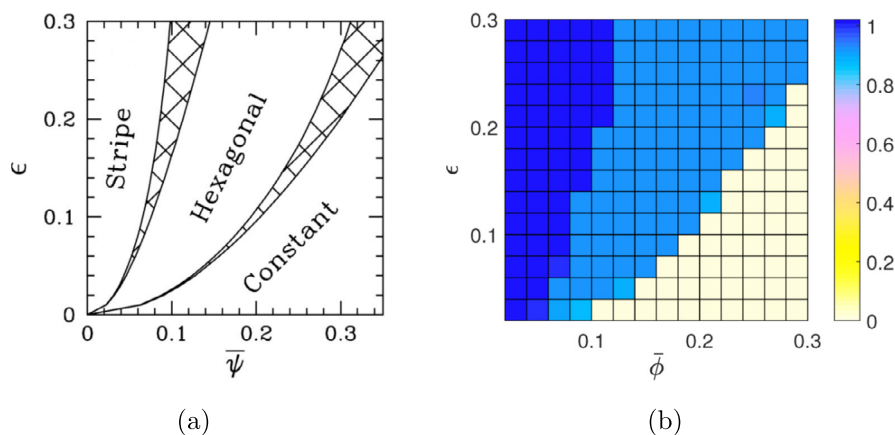


Fig. 18. Phase diagrams. Here, (a) is obtained from Elder et al. [1] and (b) is obtained from Lee [32]. Reprinted with the permission of MDPI press. In (a), the average concentration $\bar{\psi} = \bar{\phi}$.

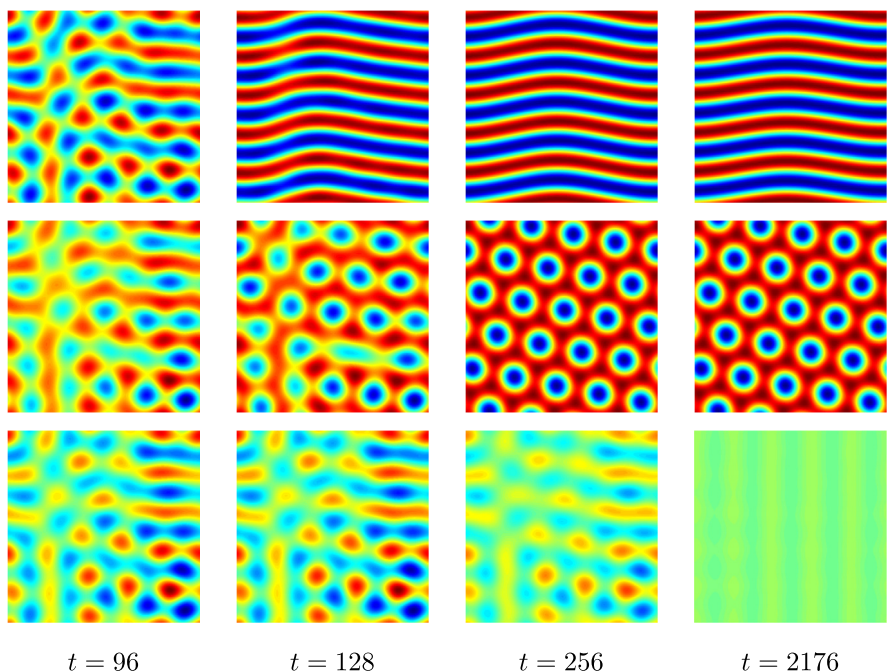


Fig. 19. Snapshots of ϕ with $(\bar{\phi}, \epsilon) = (0.02, 0.1)$ (top row), $(0.14, 0.1)$ (middle row), and $(0.26, 0.1)$ (bottom row).

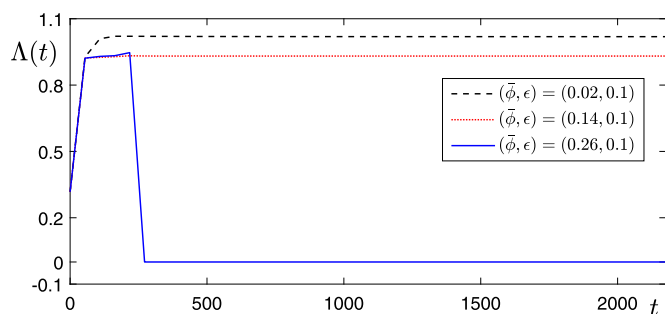


Fig. 20. Evolutions of indicator function $\Lambda(t)$ with respect to $(\bar{\phi}, \epsilon)$.

ing the original equations, a modified ESAV approach was adopted to construct an expanded system. The backward Euler, BDF2, and BDF3 approximations were considered to design temporal schemes with first-, second-, and third-order accuracies. The modified energy dissipation property for each scheme could be easily estimated. In each time step, the computation was totally decoupled and each variable could be easily updated. The numerical examples indicated that the proposed methods not only had desired accuracy and energy stability but also worked well for phase transition, crystal growth, and pattern formation. In upcoming studies, the proposed methods will be used to simulating phase-field crystal type models with complex dynamics [41–44].

Acknowledgements

The work of Z. Tan is supported by the Special Project on High-performance Computing under the National Key R&D Program of China (No. 2016YFB0200604), the National Natural Science Foundation of China (11971502), and Guangdong Province Key Laboratory of Computational Science at the Sun Yat-sen University (2020B1212060032). The corresponding author (J.S. Kim) was supported by Basic Science Research Program through the National Research Foundation of Korea (NRF) funded by the Ministry of Education (NRF-2019R1A2C1003053). The authors thank the reviewers for the constructive suggestions on the revision of this paper.

References

- [1] K.R. Elder, M. Katakowski, M. Haataja, M. Grant, Modeling elasticity in crystal growth, *Phys. Rev. Lett.* 88 (2002) 245701.
- [2] Y. Li, J. Kim, An efficient and stable compact fourth-order finite difference scheme for the phase field crystal equation, *Comput. Methods Appl. Mech. Eng.* 319 (2017) 194–216.
- [3] H.G. Lee, J. Kim, A simple and efficient finite difference method for the phase-field crystal equation on curved surfaces, *Comput. Methods Appl. Mech. Eng.* 307 (2016) 32–43.
- [4] M. Dehghan, V. Mohammadi, The numerical simulation of the phase field crystal (PFC) and modified phase field crystal (MPFC) models via global and local meshless methods, *Comput. Methods Appl. Mech. Eng.* 298 (2016) 453–484.
- [5] D.J. Eyre, Unconditionally gradient stable time marching the Cahn–Hilliard equation, in: *Computational and Mathematical Models of Microstructural Evolution*, San Francisco, CA, 1998, in: *Mater. Res. Soc. Sympos. Proc.*, vol. 529, Warrendale, PA, 1998, pp. 39–46.
- [6] J. Zhang, J. Zhao, J.R. Wang, A non-uniform time-stepping convex splitting scheme for the time-fractional Cahn–Hilliard equation, *Comput. Math. Appl.* 80 (5) (2020) 837–850.
- [7] D. Lee, The numerical solutions for the energy-dissipative and mass-conservative Allen–Cahn equation, *Comput. Math. Appl.* 80 (2020) 263–284.
- [8] Z. Hu, S.M. Wise, C. Wang, J.S. Lowengrub, Stable and efficient finite-difference nonlinear-multigrid schemes for the phase field crystal equation, *J. Comput. Phys.* 228 (2009) 5323–5339.
- [9] S.M. Wise, C. Wang, J.S. Lowengrub, An energy-stable and convergent finite-difference scheme for the phase field crystal equation, *SIAM J. Numer. Anal.* 44 (2009) 2269–2288.
- [10] Z. Guan, V. Heinonen, J. Lowengrub, C. Wang, S.M. Wise, An energy stable, hexagonal finite difference scheme for the 2D phase field crystal amplitude equations, *J. Comput. Phys.* 321 (2016) 1026–1054.

- [11] L. Dong, W. Feng, C. Wang, S.M. Wise, Z. Zhang, Convergence analysis and numerical implementation of a second order numerical scheme for the three-dimensional phase field crystal equation, *Comput. Math. Appl.* 75 (6) (2018) 1912–1928.
- [12] K. Cheng, C. Wang, S.M. Wise, An energy stable BDF2 Fourier pseudo-spectral numerical scheme for the square phase field crystal equation, preprint, arXiv:1906.12255.
- [13] J. Shin, H.G. Lee, J.-Y. Lee, Long-time simulation of the phase-field crystal equation using high-order energy-stable CSRK methods, *Comput. Methods Appl. Mech. Eng.* 364 (2020) 112981.
- [14] S. Pei, Y. Hou, B. You, A linearly second-order energy stable scheme for the phase field crystal model, *Appl. Numer. Math.* 140 (2019) 134–164.
- [15] Z. Liu, X. Li, Efficient modified stabilized invariant energy quadratization approaches for phase-field crystal equation, *Numer. Algorithms* 85 (2020) 107–132.
- [16] L. Wang, Y. Huang, K. Jiang, Error analysis of SAV finite element method to phase field crystal model, *Numer. Math. Theor. Methods Appl.* 13 (2020) 372–399.
- [17] M. Sun, X. Feng, K. Wang, Numerical simulation of binary fluid-surfactant phase field model coupled with geometric curvature on the curved surface, *Comput. Methods Appl. Mech. Eng.* 367 (2020) 113123.
- [18] C. Zhang, J. Ouyang, Unconditionally energy stable second-order numerical schemes for the functionalized Cahn–Hilliard gradient flow equation based on the SAV approach, *Comput. Math. Appl.* 84 (2021) 16–38.
- [19] Q. Li, L. Mei, Efficient, decoupled, and second-order unconditionally energy stable numerical schemes for the coupled Cahn–Hilliard system in copolymer/homopolymer mixtures, *Comput. Phys. Commun.* 260 (2021) 107290.
- [20] J. Swift, P.C. Hohenberg, Hydrodynamic fluctuation at the convective instability, *Phys. Rev. A* 15 (1977) 319–328.
- [21] M.C. Cross, P.C. Hohenberg, Pattern formation outside of equilibrium, *Rev. Mod. Phys.* 65 (1993) 851–1112.
- [22] H.G. Lee, Numerical simulation of pattern formation on surfaces using an efficient linear second-order method, *Symmetry* 11 (8) (2019) 1010.
- [23] M. Dehghan, M. Abbaszadeh, The meshless local collocation method for solving multi-dimensional Cahn–Hilliard, Swift–Hohenberg and phase field crystal equations, *Eng. Anal. Bound. Elem.* 78 (2017) 49–64.
- [24] H.G. Lee, A semi-analytical Fourier spectral method for the Swift–Hohenberg equation, *Comput. Math. Appl.* 74 (8) (2017) 1885–1896.
- [25] A.F. Sarmiento, L.F.R. Espath, P. Vignall, L. Dalcin, M. Parsani, V.M. Calo, An energy-stable generalized- α method for the Swift–Hohenberg equation, *J. Comput. Appl. Math.* 344 (2018) 836–851.
- [26] J. Su, W. Fang, Q. Yu, Y. Li, Numerical simulation of Swift–Hohenberg equation by the fourth-order compact scheme, *Comput. Appl. Math.* 38 (2019) 54.
- [27] H.G. Lee, An energy stable method for the Swift–Hohenberg equation with quadratic-cubic nonlinearity, *Comput. Methods Appl. Mech. Eng.* 343 (2019) 40–51.
- [28] H. Liu, P. Yin, Unconditionally energy stable DG schemes for the Swift–Hohenberg equation, *J. Sci. Comput.* 81 (2019) 789–819.
- [29] H. Liu, P. Yin, Energy stable Runge–Kutta discontinuous Galerkin schemes for fourth order gradient flows, preprint, arXiv:2101.00152.
- [30] H. Liu, P. Yin, On the SAV-DG method for a class of fourth order gradient flows, preprint, arXiv:2008.11877.
- [31] H.G. Lee, A new conservative Swift–Hohenberg equation and its mass conservative method, *J. Comput. Appl. Math.* 375 (2020) 112815.
- [32] H.G. Lee, An efficient and accurate method for the conservative Swift–Hohenberg equation and its numerical implementation, *Mathematics* 8 (2020) 1502.
- [33] J. Zhang, X. Yang, Numerical approximations for a new L^2 -gradient flow based phase field crystal model with precise nonlocal mass conservation, *Comput. Phys. Commun.* 243 (2019) 51–67.
- [34] Z. Liu, X. Li, The exponential scalar auxiliary variable (E-SAV) approach for phase field models and its explicit computing, *SIAM J. Sci. Comput.* 42 (3) (2020) B630–B655.
- [35] Z. Liu, X. Li, A highly efficient and accurate exponential semi-implicit scalar auxiliary variable (ESI-SAV) approach for dissipative system, preprint, arXiv:2010.11728v1.
- [36] J. Yang, J. Kim, A variant of stabilized-scalar auxiliary variable (S-SAV) approach for a modified phase-field surfactant model, *Comput. Phys. Commun.* 261 (2021) 107825.
- [37] J. Yang, J. Kim, Linear, second-order accurate, and energy stable scheme for a ternary Cahn–Hilliard model by using Lagrange multiplier approach, *Acta Appl. Math.* 172 (2021) 10.
- [38] Y. Li, C. Luo, B. Xia, J. Kim, An efficient linear second order unconditionally stable direct discretization method for the phase-field crystal equation on surfaces, *Appl. Math. Model.* 67 (2019) 477–490.
- [39] S. Yoon, D. Jeong, C. Lee, H. Kim, H.G. Lee, J. Kim, Fourier-spectral method for the phase-field equations, *Mathematics* 8 (8) (2020) 1385.
- [40] X. Yang, D. Han, Linearly first- and second-order, unconditionally energy stable schemes for the phase field crystal model, *J. Comput. Phys.* 330 (2017) 1116–1134.
- [41] Q. Li, L. Mei, Y. Li, Efficient second-order unconditionally stable numerical schemes for the modified phase field crystal model with long-range interaction, *J. Comput. Appl. Math.* 389 (2021) 113335.
- [42] B. Xia, C. Mei, Q. Yu, Y. Li, A second order unconditionally stable scheme for the modified phase field crystal model with elastic interaction and stochastic noise effect, *Comput. Methods Appl. Mech. Eng.* 363 (2020) 112795.

- [43] M. Wang, Q. Huang, C. Wang, A second order accurate scalar auxiliary variable (SAV) numerical method for the square phase field crystal equation, preprint, arXiv: 2012.15133.
- [44] H.G. Lee, J. Shin, J-Y. Lee, First- and second-order energy stable methods for the modified phase field crystal equation, *Comput. Methods Appl. Mech. Eng.* 321 (2017) 1–17.